Chinese Chemical Letters 37 (2026) 112502

Contents lists available at ScienceDirect

Chinese Chemical Letters

journal homepage: www.elsevier.com/locate/cclet

Application of heteroatom-doped carbon in peroxymonosulfate activation for enhancing Fenton-like performance: Current development, challenges and prospects

Sai Bai[a], Qianyu Pan[b], Xiangning Xu[c], Minxian Cheng[a], Xiaoming Peng[b,*], Jin Qian[a,*]

[a] Research & Development Institute in Shenzhen, School of Chemistry and Chemical Engineering, Northwestern Polytechnical University, Xi'an 710072, China
[b] School of Civil Engineering and Architecture, East China Jiaotong University, Nanchang 330013, China
[c] The Second Geological Brigade of Sichuan, Chengdu 610081, China

ARTICLE INFO

Article history:
Received 22 July 2025
Revised 7 January 2026
Accepted 5 February 2026
Available online 7 February 2026

Keywords:
Carbon-based catalysts
Peroxymonosulfate
Organic pollutants
Heteroatom-doping
Electronic density

ABSTRACT

Emerging contaminants (ECs) present significant environmental and health risks due to their widespread impact. Catalytic Fenton-like reactions using carbon-based catalysts offer a promising and sustainable solution for EC removal. This review synthesizes recent advancements in heteroatom-doped carbon (HDC) catalysts for peroxymonosulfate (PMS) activation, critically evaluating the merits and limitations of HDC-mediated Fenton-like reactions. The review explores how doping affects catalyst porosity, electronic properties, PMS activation efficiency, and overall effectiveness in EC removal. Innovative strategies for identifying key reactive species in HDC/PMS systems are discussed, including the use of chemical probes, spin-trapping agents, and SETP-based methodologies. Additionally, density functional theory (DFT) is utilized to investigate the electronic structures of ECs and their interactions with reactive oxygen species (ROS). The practical potential of HDCs in remediating contaminated groundwater and wastewater is also addressed, alongside a discussion of the challenges and future research directions to enhance their scalable applications, offering a roadmap for advancing sustainable environmental remediation technologies.
© 2026 Published by Elsevier B.V. on behalf of Chinese Chemical Society and Institute of Materia Medica, Chinese Academy of Medical Sciences.

1. Introduction

A wide range of emerging contaminants (ECs)—including pharmaceuticals, personal care ingredients, endocrine-active compounds, dyes, and microplastics—are now routinely reported in natural and engineered waters, drawing increasing scientific concern [1]. Owing to their high persistence and propensity for bioaccumulation, these pollutants pose substantial risks to both human health and aquatic ecosystems. Exposure can impair biological functions and has been associated with chronic toxic outcomes, such as carcinogenic, teratogenic, and mutagenic effects. To address these challenges, advanced oxidation processes (AOPs) have been intensively explored for wastewater treatment. By *in situ* generating highly reactive oxidants, AOPs can transform refractory organic matter into smaller, less persistent molecules, thereby reducing overall toxicity [2,3].

AOPs, widely employed for the degradation of ECs, primarily include Fenton oxidation, peroxymonosulfate (PMS)-based oxidation, and ozonation, each relying on distinct mechanisms for generating reactive oxygen species (ROS) [4–7]. Among these, sulfate radical-based advanced oxidation processes (SR-AOPs) have attracted substantial interest because of their operational robustness, strong oxidative capability, and adaptability over a wide pH window [8]. PMS-AOPs are especially appealing for wastewater remediation, as producing sulfate radicals ($SO_4^{\bullet-}$), hydroxyl radicals ($^{\bullet}OH$), and singlet oxygen ($^1O_2$). PMS with asymmetric molecular structure could be converted to $SO_4^{\bullet-}$ through homogeneous or heterogeneous activation [9]. The redox potential, dissociation energy and O–O bond length in PMS are 1.82 V, 377 kJ/mol, and 1.460 Å, respectively, which makes it beneficial for oxidizing ECs [10].

In recent years, carbonaceous materials, have garnered significant attention as effective activators of PMS. Owing to the inherent metal-free nature, exceptional stability, tunable physicochemical properties, and large specific surface area (SSA) [11]. The incorporation of heteroatoms (*e.g.*, sulfur (S), boron (B), nitrogen (N), phosphorus (P)), into the carbon matrix has proven to significantly enhance the catalytic properties of carbon-based catalysts. Heteroatom-doping not only overcomes the intrinsic inertness of pure carbon catalysts but also modulates the electroactive sites within the carbon framework, thereby improving the chemical sta-

* Corresponding authors.
E-mail addresses: pengxiaoming70@126.com (X. Peng), qianjin@nwpu.edu.cn (J. Qian).

https://doi.org/10.1016/j.cclet.2026.112502
1001-8417/© 2026 Published by Elsevier B.V. on behalf of Chinese Chemical Society and Institute of Materia Medica, Chinese Academy of Medical Sciences.

bility and enabling fine control over the catalytic pathways in SR-AOPs [12]. The electronegativity, charge density, and size of the doped heteroatoms play pivotal roles in optimizing catalytic performance. By introducing electron-rich or electron-deficient atoms, the surface charge distribution of carbon materials can be altered, while the defects created during the doping process serve as novel active sites, further enhancing the catalytic efficiency. Notably, compared to metal-based catalysts, heteroatom-doped carbon materials offer distinct advantages, including lower cost, superior stability, and minimal environmental impact. These benefits position heteroatom-doped carbon materials as highly promising alternatives in the activation of PMS for environmental remediation applications [13,14].

This review offers an up-to-date summary of the progress in heteroatom-doped carbon (HDCs) catalysts for the removal of persistent organic pollutants in water, with a specific emphasis on PMS activation. HDCs-based catalysts are classified into single-doped and multi-doped porous carbon catalysts. This review covers several key topics, including the effects of heteroatom doping, the PMS activation mechanism, and the practical application potential in wastewater treatment. These insights aim to guide the rational design of efficient metal-free carbonaceous catalysts for EC abatement *via* PMS activation. Moreover, current limitations and future directions are highlighted, including the use of machine learning (ML) to deeply investigate PMS activation mechanism with HDCs-based catalysts, long-term durability, evaluation of the environmental impact of HDCs in PMS activation process are also discussed.

2. Effect of heteroatom doping on porous carbons

2.1. Effect of single heteroatom doping

Introducing heteroatoms (*e.g.*, N, B, S, and P) into carbon frameworks is an effective route to tune the reactivity of porous carbon catalysts. The integrated heteroatoms, with varying atomic radius, orbitals, electron density and electronegativity, their incorporation perturbs the local electronic structure of the sp^2 carbon lattice and breaks its intrinsic inertness, thereby generating catalytically active motifs that can facilitate PMS activation [15].

2.1.1. Nitrogen doping

Nitrogen doping is widely adopted because its atomic size is close to that of carbon (0.65 Å for N *vs.* 0.77 Å for C), enabling high dopant incorporation, while its higher electronegativity (3.04 for N *vs.* 2.55 for C) provides an efficient means to regulate local electronic structures [16]. As a representative strategy for metal-free carbon catalysts, N incorporation can (i) reconfigure the electronic environment of nearby carbon atoms to generate new functionalities and catalytic sites, (ii) activate adjacent sp^2 carbon by facilitating π-electron redistribution, and (iii) enhance charge delocalization, thereby alleviating the intrinsic inertness of the carbon lattice [17]. In parallel, N dopants markedly reshape the spin density and charge distribution of surrounding carbon atoms, often accompanied by local bond perturbations and lattice distortion that elevate chemical reactivity during catalysis [18,19]. N dopants also introduce electron-rich Lewis basic sites in graphitic carbons, enhancing coordination in redox processes and promoting PMS activation [20]. Additionally, N doping enhances both adsorption and PMS activation performance, effectively aiding in the removal of antibiotics from water [21].

The specific nitrogen species responsible for improved catalytic performance in PMS activation remain unclear. In N/PMS systems, various nitrogen configurations, including pyrrolic-, pyridinic-, amino-, and graphitic-N, have been proposed as potential active centers. Thus, understanding the role of N-doping in Fenton-like reaction is essential for designing targeted carbon catalysts for PMS-AOP systems. While graphitic-, pyrrolic-, and pyridinic-N have been shown to enhance PMS activation, nitrogen oxides are ineffective for this process [22]. Graphitic-N is sp^2-hybridized, bonded to three sp^2 carbon atoms. Theoretical studies show it has the lowest PMS adsorption energy and highest electron transfer capacity among N dopants [23]. This superior performance likely stems from nitrogen's higher electronegativity, which enables it to modify the charge distribution of nearby carbon atoms. This adjustment enhances electronic properties and promotes efficient electron transfer, crucial for catalytic processes [24]. As a result, the polarized carbon atoms adjacent to graphitic N interact strongly with PMS, weakening the O–O linkage and promoting bond cleavage [12,25]. Pyrrolic-N is formed by incorporating one nitrogen atom into a five-membered heterocyclic ring, while pyridinic-N is created by integrating sp^2-hybridized nitrogen in a six-membered ring [26]. Pyridinic- and pyrrolic-N, possessing lone-pair electrons similar to those in ketones, function as Lewis-base sites. These sites can interact with electrophilic species from peroxides, thereby activating PMS and generating ROS [27]. Duan *et al.* employed N-doped carbon nanotubes (NCNTs) to enhance PMS-driven phenol removal. Compared to undoped single-walled carbon nanotubes (SWCNTs), the catalytic efficiency of N-doped SWCNTs was enhanced from 56.5% to 100%, with k value significantly increased from 0.0043 min^{-1} to 0.2466 min^{-1}. This improvement is attributed to the reduced oxygen content and the introduction of graphitic nitrogen *via* high-temperature nitrogen doping, which creates defect sites and enhances electron transfer from adjacent carbon atoms.

2.1.2. Boron doping

Boron (B) atom has similar atomic radius (0.85 Å *vs.* 0.77 Å of carbon) and smaller electronegativity ($\chi_B = 2.04 < \chi_C = 2.55$) compared to carbon atom, indicating that it can be easily doped into the carbon matrix and can serve as acceptor of π-electron [28]. The introduction of boron into the carbon matrix alters the electronic structure of the carbon network. Since the boron atom has only three valence electrons-with two in the 2s orbital and one in the 2p orbital-it creates electron-deficient sites within the carbon lattice. Doping with B atom could activate the π-electrons of both the B and adjacent C atoms, creating "holes" that facilitate charge migration, thereby enhancing the electrical conductivity of HDCs-based catalysts [29]. Relevant reports indicate that B-doped carbon enhances PMS activation by facilitating the adsorption of PMS and interacting with various contaminants, such as bisphenol A and tetracycline.

Specifically, the configurations of B-doping atom in carbon matrix include BC_3 and oxidized B (CBO_2 and C_2BO), these structures endow the catalysts with PMS activation property. The BC_3 moiety forms when B atom replaces a C atom in the sp^2 carbon structure, which is considered as the optimal bonding configuration for enhancing the catalytic capacity of carbon materials. Additionally, the CBO_2 and C_2BO moieties facilitate PMS activation *via* the nonradical pathway, with $^1O_2$ serving as dominant active species generated during reaction. Moreover, the BCO_2 and BC_2O motifs are proposed as catalytically active sites that facilitate PMS activation by strengthening the interfacial interaction between PMS and boron-doped ordered mesoporous carbon (B-OMC) [30].

2.1.3. Sulfur doping

Sulfur (S), with an electronegativity of 2.58 (compared to C of 2.55) and a greater atomic size (1.04 Å *vs.* 0.77 Å for C), has garnered significant attention in recent years for its role in PMS activation and pollutant degradation [31,32]. Experimental and theoretical results show that S-doping configurations in the carbon matrix are thiophene S and oxidized S, which depend on pyrolysis temperature and synthesis methods. Higher pyrolysis tempera-

tures promote the conversion of oxidized S to thiophene S, though excessively high temperatures can reduce sulfur content due to C-S bond cleavage [33].

Thiophene S refers to S atoms bonded to aromatic rings in the sp^2-C system, acting as key catalytic sites in the S-doping carbon catalysts/PMS system. The electron-rich thiophene S, as a Lewis basic site, can activate PMS *via* radical pathway, generating $^{\bullet}OH$ and $SO_4^{\bullet-}$ [34]. In the non-radical pathway, thiophene sulfur boosts charge density of adjacent carbon atoms, generates defects, and promotes charge delocalization, enhancing electron transfer and activating sp^2-hybridized carbon for PMS activation [35]. Conversely, oxidized S, with electron-withdrawing properties, inhibits acidic organic adsorption and limits electron transfer, reducing PMS activation efficiency [36]. S atoms, particularly in the thiophene configuration, enhance electron density and facilitate electron transfer, crucial for PMS activation. However, S atoms may leach from the carbon matrix during PMS activation, especially in acidic environments, potentially introducing secondary pollutants into the treated water [37]. XPS analysis of sulfur before and after the reaction was conducted to investigate sulfur leaching during PMS activation. Further analysis of the S 2p high-resolution spectra reveals a decrease in the thiophene-S (C-S-C) content at 163.9 eV and 165.0 eV, along with an increase in sulfur oxides at 168.1 eV. This transformation suggests that sulfur leaching occurs during PMS activation, which may weaken the catalytic activity of the material. As reported by Liu *et al.*, who reported sulfur leaching and the conversion of sulfur-containing species during activation, which in turn affected the catalytic performance [38]. These findings underscore the role of sulfur leaching and the transformation of sulfur species in determining the efficiency of subsequent activation cycles.

2.1.4. Phosphorus doping

Compared to C atom, P atom has lower electronegativity (2.19 *vs.* 2.55 of C) and larger atomic radius (1.00 Å *vs.* 0.77 Å of C). As a result, P incorporation typically behaves as an n-type electron donor within conjugated carbon frameworks; however, it differs fundamentally from N doping because its valence electrons reside in the third shell [39]. The introduction of P into the carbon skeleton facilitates charge delocalization, disrupts electron distribution, and generates more defective sites within the structure [40]. Moreover, P doping can enhance the oxidation resistance of the carbon network by introducing negative charges to adjacent C atoms, thereby forming electron clouds. This electron density redistribution improves the stability of the carbon structure, protecting it from oxidative environments. This effect has been widely reported in the literature, where phosphorus doping has been shown to strengthen the carbon matrix's resistance to oxidation by modulating the electronic properties of the carbon framework [41,42]. Furthermore, the adsorption ability of HDCs-based catalysts for different pollutants is notably enhanced by the formation of π-π interactions and hydrogen bonds [43].

2.2. Effect of heteroatom co-doping

Single heteroatom doping introduces unique characteristics to carbon materials, optimizing their structure for specific applications in PMS-based catalysis. In co-doped carbon catalysts, the simultaneous incorporation of boron, nitrogen, and sulfur creates notable asymmetry, which significantly influences the charge distribution and density within the carbon framework [44–46]. Consequently, the interaction of different heteroatoms can create a synergistic effect, improving the overall performance of co-doped metal-free carbonaceous catalysts.

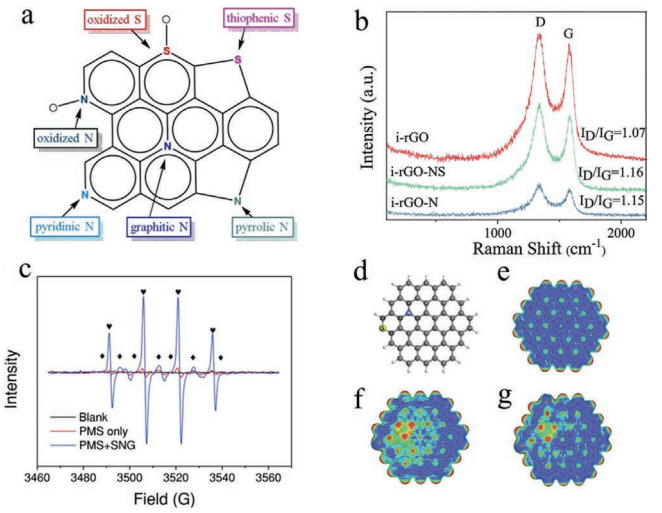


Fig. 1. (a) Structural configurations and (b) Raman spectra of N,S-co-doping carbon materials. Reprinted with permission [47]. Copyright 2019, Elsevier. (c) EPR spectra in N,S-co-doping/PMS system (♥: DMPO-$^{\bullet}$OH, ♦: DMPO-$SO_4^{\bullet-}$). (d) Optimized N,S-co-doping model graphene. Electrostatic potential mapping from charge density matrix for (e) undoped model graphene, (f) S-N-G and (g) S-S-N-G configurations. Reprinted with permission [44]. Copyright 2015, Wiley-VCH.

2.2.1. Nitrogen and sulfur co-doping

N and S co-doping is one of the most extensively studied strategies for modifying carbon materials. In N,S co-doped catalysts, the nitrogen atom has greater electronegativity compared to carbon, while the sulfur atom possesses larger, more polarizable valence orbitals. The incorporation of both N and S into the carbon lattice substantially modifies the physical and chemical properties of the carbon-based catalysts. Various configurations of N,S-co-doping are illustrated in Fig. 1a. Sun *et al.* synthesized heteroatom-doped graphene oxide using a thermal decomposition method and assessed the structural disorder by evaluating the I_D/I_G ratio based on Raman spectroscopy (Fig. 1b) [47]. Heteroatom-doping could significantly enhance the degree of defect with the co-doping with N and S (i-rGO–NS) showed the highest, higher than single N-doped rGO and pristine rGO, indicating the co-doping of i-rGO with N, S could introduce defects into carbon substrate and thus may have a certain impact on catalytic properties. Recently, Duan *et al.* have tried to use diphenyl disulfide and ammonium nitrate to introduce S and N to reduced graphene oxide (rGO), obtaining S,N-rGO [44]. The co-doped S, N-rGO also showed a significant enhancement in catalytic-degradation performance of phenol by PMS activation through radical pathways involving the generation of $SO_4^{\bullet-}$ and $^{\bullet}OH$ (Fig. 1c). Electrostatic potential mapping (ESP) reveals that N,S-doping charges adjacent carbon atoms positively, creating active sites for HSO_5^- adsorption and O–O bond cleavage (Figs. 1d–g).

Co-doping substitutional S with graphitic N increases charge and improves PMS adsorption performance [48]. Duan *et al.* showed that thiophene S and graphitic N interactions regulate the charge and spin density of neighboring carbon atoms [49]. However, pyrrolic or pyridinic N and S co-doping reduces porosity due to pore blockage, as noted by Shi *et al.* [50]. Graphitic-N promotes electron flow and adjusts the electron density of adjacent carbon atoms, while electron-rich thiophene-S increases the asymmetric spin charge density of nearby carbon atoms. As a result, the synergistic effect of N and S significantly enhances the cleavage of the O–O bond in PMS, with singlet oxygen ($^1O_2$) playing a dominant role in the degradation of bisphenol A (BPA). This synergy achieves a BPA removal efficiency of 98.4% within 60 min. Similar non-radical pathway dominated system was further conducted by

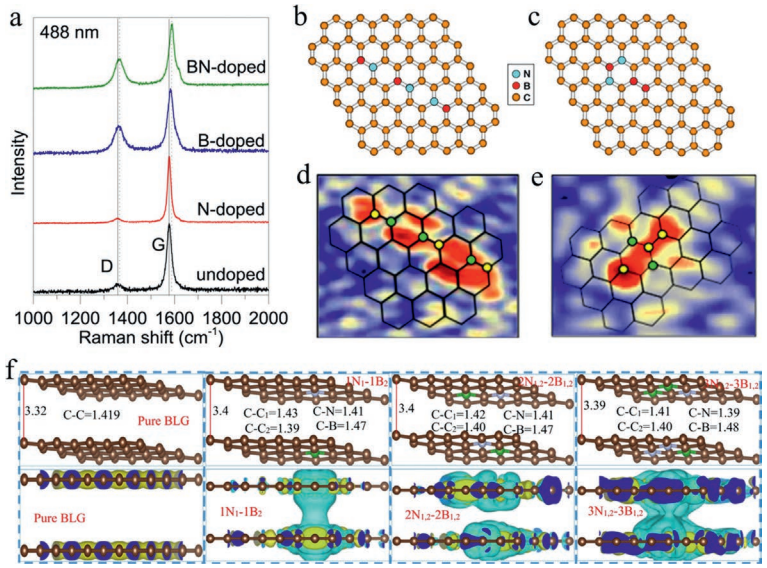


Fig. 2. (a) Raman spectra of N,B-doped CNTs. Reprinted with permission [51]. Copyright 2018, Elsevier. Visual structure of (b) B-N-C–C and (c) B-B-C–N bond configurations. (d, e) Simulated STM images; Reprinted with permission [53]. Copyright 2016, American Chemical Society. (f) Structure diagrams and charge density differences of bilayer graphene (BLG) incorporated with varying N and B atoms. Reprinted with permission [54]. Copyright 2019, Elsevier.

Li *et al.* with introducing the S atom to nitrogen-doped graphene (S,N-G) [45].

2.2.2. Nitrogen and boron co-doping

B atoms have fewer valence electrons than that of N atoms, which influences the bonding behavior and electronic properties, especially after incorporating into carbon-based structures. Sedelnikova *et al.* have prepared the N,B-doped carbon nanotubes (CNTs) by evaporation of solid graphite rod in various atmosphere with arc-discharge processing. N,B-doped CNTs samples are always enriched with short CNTs and polyhedral nanoparticles, suggesting that the incorporation of N and B into graphite electrode results in disordering of graphitic structure. Raman spectra (Fig. 2a) could be further confirmed the conclusion above due to the improved I_D/I_G of N,B-doped CNTs, indicating the enriched defects and functionalities with N,B-doping. Moreover, for the N,B-doped samples, a significant upshift of D band (1358 cm^{-1}) and G band (1577 cm^{-1}), which are more probably attributed to the holes doping during the synthesis process [51].

Introducing N and B simultaneously into carbon frameworks can markedly perturb the local electronic structure, often generating electron-deficient domains that are beneficial for catalysis while also improving thermal robustness [52]. In such co-doped lattices, B incorporation reinforces the sp^2 carbon network, whereas N, owing to its higher electronegativity, withdraws electron density and can redistribute charge toward neighboring B sites through the conjugated carbon bridge. As a result, adjacent B–N pairs are energetically favored (stabilized by ~2.35 eV), whereas B–B and N–N pairings are comparatively unfavorable. Schiros *et al.* directly resolved these B–N bonding motifs in monolayer graphene by combining synchrotron X-ray characterization, scanning tunneling microscopy (STM), and DFT calculations, revealing distinct local configurations and corresponding changes in the local density of states [53]. As depicted in Figs. 2b and c, multiple local bonding motifs (*e.g.*, B–N–C–C and N–B–C–N) were identified, and STM images further corroborated the atomic-scale arrangements of these co-dopant complexes (Figs. 2d and e). In parallel, the spectroscopic/STM analysis indicated pronounced dopant-induced perturbations in the local density of states arising from the incorporated heteroatoms.

The concentration of N and B atoms during synthesis influences the structural and electronic properties. Rafique *et al.* found that B and N doping in bilayer graphene (BLG) increases the interlayer distance from 3.32 Å to 3.4 Å. Higher B concentrations shorten C–C bonds and elongate B-C bonds (1.46–1.48 Å), while more N atoms lengthen C–C bonds and shorten N–C bonds (Fig. 2f). The charge density difference (CCD) increases with higher doping, with N atoms donating electrons (n-type) and B atoms attracting electrons (p-type), affecting the charge transfer between BLG layers [54]. N and B co-doping synergistically enhances PMS activation by improving electron transfer, reducing PMS adsorption energy, and prolonging O–O bond cleavage, promoting free radical generation. Chen *et al.* synthesized N and B co-doped graphene oxide (GO) for PMS activation in sulfacetamide degradation, with tunable doping levels and N-B configurations through annealing [46].

2.2.3. Nitrogen and phosphorus co-doping

Similar to N atoms, P atoms with five valence electrons can donate electrons, altering the electron distribution of the substrate. Owing to its lower electronegativity and larger atomic size, P acts as a stronger electron donor in conjugated carbon structures [55]. P-incorporation creates more defect sites in the carbon lattice, which can strengthen $\pi-\pi$ interactions between aromatic molecules and graphitic domains, ultimately benefiting catalytic performance [56]. Xin *et al.* developed N/P co-doped ordered mesoporous carbon (NPMC) using a sol-gel method. Compared to N-doped (NMC), P-doped (PMC), and undoped (OMC) carbon, NPMC exhibited a higher I_D/I_G ratio, indicating increased disorder and defects in the carbon framework (Fig. 3a) [57]. The numerous structural defects in NPMCs generate additional active sites, boosting electrochemical performance. Qiao *et al.* investigated the electrocatalytic activity of P,N-co-doped reduced graphene oxide (PN-rGO), which exhibited the superior current density at −0.96 mA/cm^2 (Fig. 3b). This value was approximately four times higher than that of GCE. LSV curves (Fig. 3c) further demonstrated the more positive potential of P/N co-doped graphene oxide [58].

Attributing to the electron-donating properties of N and P, co-doping may exhibit unexpected tunes on the electronic density of carbon substrate. As shown in the electrostatic potential plots (ESP, Figs. 3d–f), N atoms (blue color) of N-doped graphene (NG)

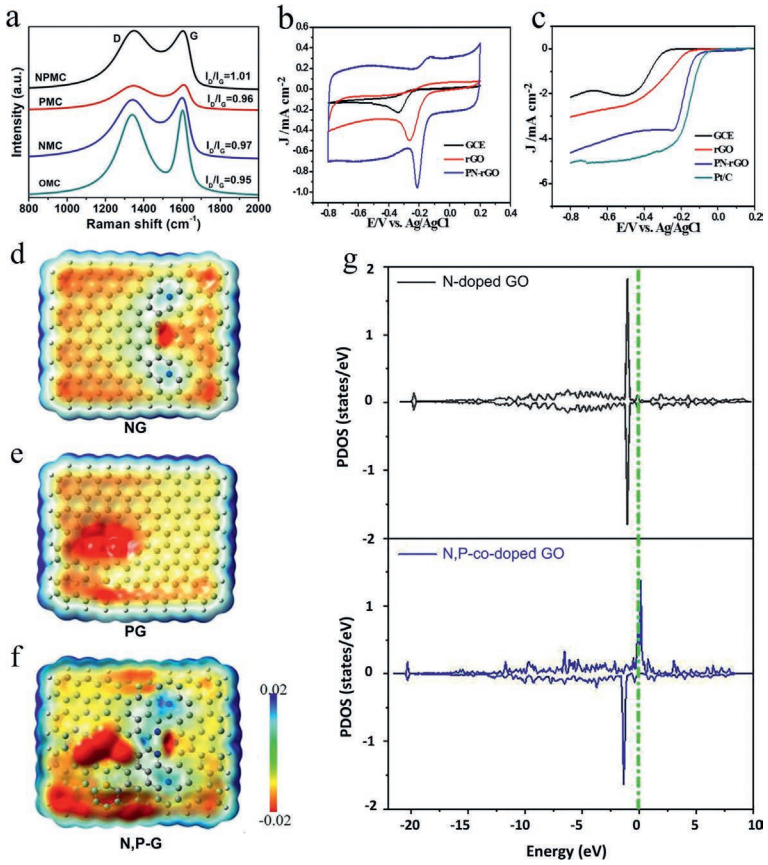


Fig. 3. (a) Raman spectra of N,P-doped mesoporous carbon materials. Reprinted with permission [57]. Copyright 2020, Elsevier. (b) CV and (c) LSV curves for N,P-doped GO. ESP mappings for (d) N-doped graphene, (e) P-doped graphene, and (f) N,P co-doped graphene, with C, H, O, N, and P atoms colored in gray, white, red, blue, and orange, respectively. (g) PDOS for N-doped GO and N,P co-doped GO models. Reprinted with permission [59]. Copyright 2020, Elsevier.

were positively charged, while P atoms (red color) were negatively charged in P-doped graphene (PG). Compared to NG and PG, the electrostatic potential of N,P-doping graphene (N,P-G) shows a large negative value around P atoms (red regions) and a positive potential around N atoms (blue regions). This suggests that N,P co-doping increases the potential difference in graphene, enhancing electron transfer performance [57]. To further investigate the electronic enhancement induced by P atom. Chen *et al.* performed partial density of state (PDOS) calculations on N-doped graphene oxide (GO) and N,P-co-doped GO (Fig. 3g). Their results showed that the states near the Fermi level of pyridine N are split in N,P-co-doped GO than that of N-doped GO. This splitting, induced by P atoms significantly increases the reactivity of pyridine N, leading to stronger adsorption towards PMS or other target pollutants [59]. Fu and colleagues further demonstrated that P/N co-doped carbon sheets are highly efficient for TC degradation through the adsorption and activation of PMS, with P played an vital role in regulating the electronic structure [60].

3. Activation mechanism of heteroatom-doped porous carbon materials

Identifying various ROS and other reactive species is essential for optimizing the PMS activation process [61]. This section summarizes the experiments and characterization techniques for understanding the mechanisms of HDCs in SR-AOPs. The radical pathway involves PMS activation and pollutant degradation *via* $SO_4^{\bullet-}$, $^{\bullet}OH$ and $O_2^{\bullet-}$ at active sites. The non-radical pathway includes singlet oxygen ($^1O_2$) produced by surface functional groups, and surface electron transfer, where the catalyst mediates electron flow between pollutants and PMS or facilitates direct oxidation *via* reactive species [62].

3.1. Identification of the working ROS

3.1.1. Chemical quenching and quantification

Selecting appropriate quenchers for the target system is crucial for identifying ROS (Table S1 in Supporting information) [63]. To assess the effectiveness of the selected scavenger, a competition kinetic rate coefficient (f) was proposed and utilized by Ren *et al.* (Text S1 in Supporting information) [64]. The quencher nearly eliminates the target ROS when the theoretical f value is <0.01. PMS-AOPs/HDCs always appeared through a synergistic mechanism, which consisting of radical species ($^{\bullet}OH$, $SO_4^{\bullet-}$, $O_2^{\bullet-}$) and non-radical species ($^1O_2$ dominated) (Fig. 4a) [65]. Hence, isolated quenching experiments alone are not sufficient to effectively investigate the reactive species presented in the system. Take the $^1O_2$ quenching for example, most $^1O_2$ scavengers including furfuryl alcohol (FFA) and L-histidine (L-His) may react directly with the PMS, $^{\bullet}OH$ and $SO_4^{\bullet-}$ at the high concentration, which may further overestimating the contribution of $^1O_2$ in the certain system [66].

Therefore, additional strategies are employed to further investigate the role of various reactive species. For example, by solving kinetic equations, the concentration of specific reactive species can be inferred. Using reported rate constants for these species, the concentrations of $^{\bullet}OH$, $SO_4^{\bullet-}$ and $^1O_2$ can be determined (Text S2 in Supporting information). Furthermore, the contribution of various ROSs could be also employed to evaluate the catalytic perfor-

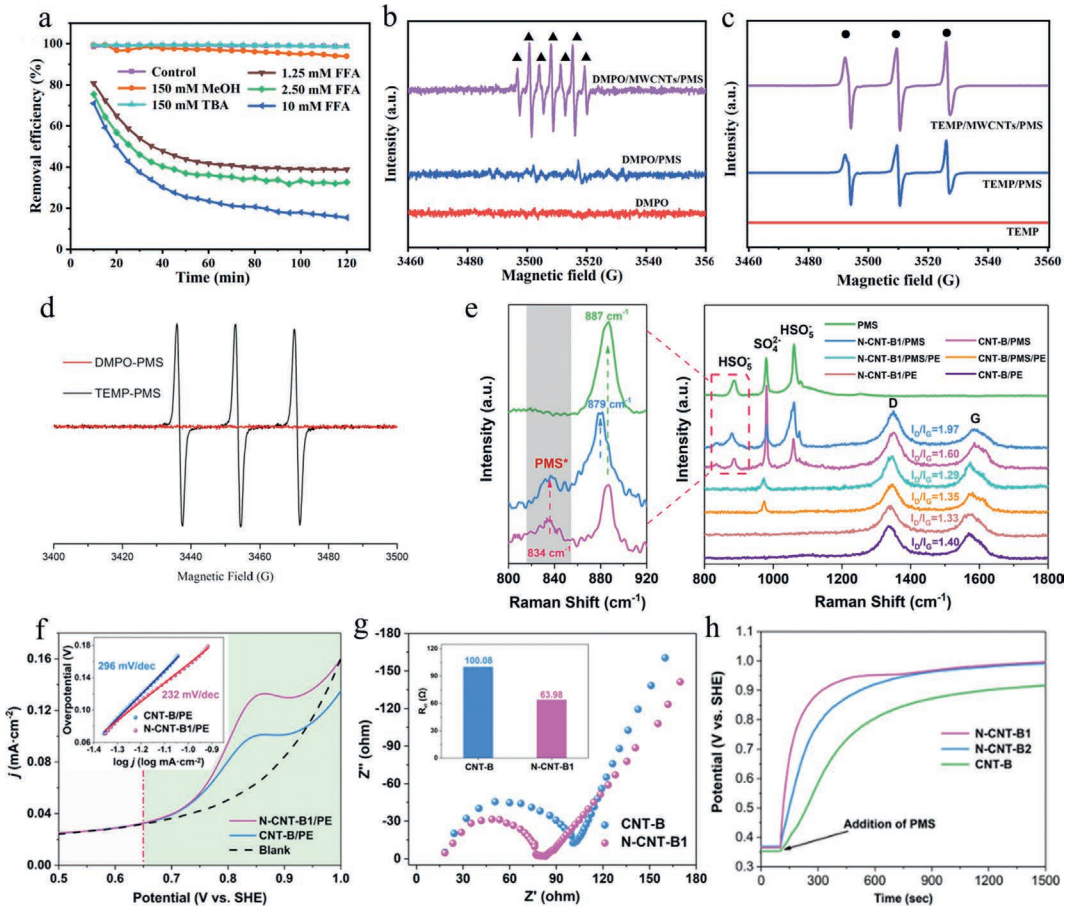


Fig. 4. (a) Removal of styrene in the presence of various quenchers. EPR spectra of (b) DMPO-$^{\bullet}$OH/$SO_4^{\bullet-}$ and (c) TEMP-$^1O_2$. Reprinted with permission [65]. Copyright 2022, American Chemical Society. (d) EPR spectra of DMPO-PMS and TEMP-PMS. Reprinted with permission [70]. Copyright 2017, Elsevier. (e) *In-situ* Raman spectra of PMS activation process. (f) LSV, (g) EIS, and (h) OCP of heteroatom-doped porous carbon materials. Reprinted with permission [15]. Copyright 2020, American Chemical Society.

mance based on the second-order constant between organic pollutants and ROSs (Text S3 in Supporting information). As summarized in Table S2, molecular electrostatic potential (MEP) surfaces were obtained from DFT calculations at the B3LYP/6–311+G* level. The blue regions present positive molecular electrostatic potential, the red regions corresponding to the negatively charged potential, and the white regions denote neutrally charged regions. Reactive radicals and non-radical oxidants can engage pollutants through different transformation routes, and the prevailing pathway is largely dictated by the contaminant's molecular structure. In radical systems, both $SO_4^{\bullet-}$ and $^{\bullet}$OH typically oxidize organics through hydrogen abstraction, electron-transfer steps, and addition reactions to unsaturated moieties. However, the structure of the pollutants plays a critical role in determining which mechanism dominates. For example, when $SO_4^{\bullet-}$ reacts with aliphatic carboxylic compounds, the first step involves electron abstraction from the oxygen atom in the carboxyl group to $SO_4^{\bullet-}$ itself. This structural characteristic facilitates the electron transfer process. On the other hand, $^{\bullet}$OH tends to abstract H atoms from the α-position of aliphatic chains, underscoring that both molecular architecture and functional-group location strongly govern radical reactivity. The nonradical species $^1O_2$, in particular, demonstrates a highly selective electrophilic addition mechanism. The reaction pathway of $^1O_2$ depends heavily on the structural features of the target molecule. For an isolated double bond, $^1O_2$ reacts *via* cycloaddition. However, allylic hydroperoxides generated *via* double bonds linked to polar hydrogen-containing functional groups. For pollutants containing conjugated dienes, $^1O_2$ engages in the Diels-Alder reaction to form endoperoxides.

Except for quenching experiments, several commonly-used chemical probes, such as 9,10-diphenylanthracene (DPA) and 9,10-anthracenediyl-bis(methylene)dimalonic acid (ABDA) are utilized to quantify the $^1O_2$, which exhibit characteristic peak wavelengths at 378 nm and 400 nm, respectively [67]. ABDA has been suggested as a semi-quantitative indicator of $^1O_2$ in PMS-AOP systems [68].

Upon reacting with $^1O_2$, it forms an endoperoxide (ABDA–O_2) that can be separated by liquid chromatography and confirmed by high-resolution mass spectrometry. In addition, singlet oxygen sensor green (SOSG)—a commercial anthracene/fluorescein-based probe—has been widely used to detect $^1O_2$ in aqueous media and biological samples, producing a fluorescence signal at ~525 nm after trapping $^1O_2$; its applicability in PMS-driven systems has also been demonstrated by Shao *et al.* [69].

3.1.2. Characterization techniques of ROS

Electron paramagnetic resonance (EPR), has been conducted to investigate the ROS *via* employing particular trapping agents (Figs. 4b–d) [65,70]. Currently, 5,5-dimethyl-1-pyrroline *N*-oxide (DMPO) is widely selected as the $^{\bullet}$OH, $SO_4^{\bullet-}$ trapping agent, with a seven-peaks demonstrating the presence of DMPO transformation product, further confirming the co-exist of $^{\bullet}$OH and $SO_4^{\bullet-}$ [71]. DMPO dissolved in $^{\bullet}$OH and $SO_4^{\bullet-}$ scavengers *e.g.*, dimethyl sulfoxide (DMSO), methanol (MeOH) and ethanol (EtOH) could further serve as the trapping agent for $O_2^{\bullet-}$, which appears in the form of six-characteristic peak signal (DMPO–$O_2^{\bullet-}$ signal) [72]. 2,2,6,6-Tetramethylpiperidin (TEMP) serves as the spin agent for $^1O_2$, with the characteristic triplet peaks of TEMP-$^1O_2$ [73].

Additionally, *in-situ* Raman spectroscopy serves as effective techniques for real-time tracking the formation and transformation of ROS and other PMS intermediates, providing insights into the PMS activation mechanism [74]. As shown in Fig. 4e, the pristine O–O bond of PMS (887 cm^{-1}) showed a blue-shifted vibration peak at 879 cm^{-1} in PMS* ($HO–OSO_3^-$), attributing to the strong interaction between PMS* and catalysts (CNT-B, N–CNT-B). Additionally, a stronger peak was observed in N–CNT-B/PMS system than that in CNT-B/PMS system, indicating that heteroatom-doping could regulate the electronic structure, thereby enhancing PMS activation. With phenol (PE) addition, the peaks of PMS and PMS* disappeared, leaving only the peak of SO_4^{2-} (979 cm^{-1}), further indicating the decomposition of PMS [15].

3.2. Identification of the surface electron transfer process (SETP)

3.2.1. Chemical quenching of SETP

Apart from the ROS, electrons could be transferred directly from the pollutants to the HDCs, leading to PMS activation. Recent studies conducted two typical mechanisms about surface electron transfer process (SETP) in SR-AOPs/HDCs systems: (1) Pollutants transfer electrons to HDCs, which then pass them to PMS (employing catalysts as the carbon bridge, pollutants as electron donor, and PMS as the electron acceptor); (2) Direct contact between PMS and HDCs forms active complexes (HDCs-PMS*) *via* SETP, which interact with pollutants to facilitate oxidation or reduction [75].

Owing to the improved electronic performance of carbonaceous catalysts with diverse heteroatom bond configurations introduced, SETP also plays an equally vital role in the SR-AOPs system [76]. More specifically, SETP can be divided into two types: inner-sphere and outer-sphere, depending on the interaction between the reactants and the substrate (HDCs) [77]. In inner-sphere interactions, reactants are strongly adsorbed on the surface of HDCs, forming direct chemical bonds. In contrast, outer-sphere interactions involve weaker adsorption, primarily governed by electrostatic forces [78]. Based on this, it is easier to distinguish the inner or outer sphere interactions by ion interference experiments during PMS or organic pollutants [79]. Perchlorate (ClO_4^-), as a typical high ionic strength solution, embraces less impact on PMS or organic pollutants adsorption through inner-sphere interactions. Contrarily, outer-sphere interactions are more sensitive to variations in ionic strength due to the changes in surface charge of the catalyst [64].

3.2.2. Characterization techniques for SETP

Online electrochemical analysis can offer direct evidence to verify the SETP mechanism in SR-AOP/HDCs systems by applying a catalyst-Nafion mixture onto the glassy carbon electrode (GCE). Typical electrochemical methods could be utilized to validate the SETP in SR-AOPs/HDCs systems, *e.g.*, linear sweep voltammetry (LSV), cyclic voltammetry (CV), electrochemical impedance spectroscopy (EIS), open circuit potential (OCP), and galvanic oxidation process (GOP) [64,80]. LSV is used to study SETP in SR-AOP/HDCs systems. The adsorption of excess reactants (PMS or organic pollutants) on the catalyst surface affects charge transfer resistance (R_{ct}) and open circuit potential, distorting current signals. The NGC800/PMS/BPA system demonstrated significantly enhanced real-time current generation with increasing potential, outperforming the NGC800 system. Additionally, the N-doped carbon nanotube exhibited a similarly high current response compared to CNT, further demonstrating the improved electron conductivity due to heteroatom doping in porous carbon materials (Fig. 4f) [15]. CV curves are also extensively used to access electrochemical reversibility. Qi *et al.* tested the CV curves of pristine activated carbon (AC-850) and S-doped activated carbons (ACS-850), showing that heteroatom-doping process significantly enhanced both oxidation and reduction capabilities, resulting in an

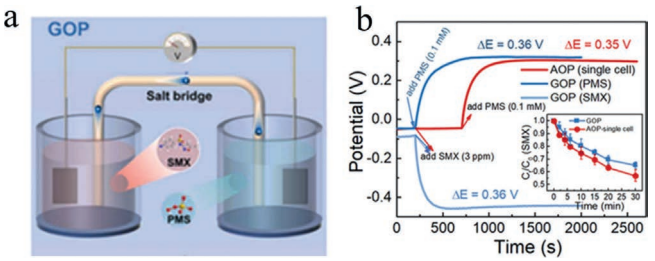


Fig. 5. (a) Schematic illustration of galvanic oxidation process (GOP). (b) OCP measurement and SMX degradation in the GOP reaction systems. Reprinted with permission [82]. Copyright 2023, Elsevier.

improved oxidation potential (~0.85 eV) and reduction potential (~0.52 eV) during the SETP process [81]. Incorporating N dopants into carbon-based materials could facilitate the interfacial reactions due to the lower impedance in charge-migration process with decreasing radius of N–CNT-B1 (R_{ct} = 63.98 Ω) compared with CNT-B (R_{ct} = 100.08 Ω) (Fig. 4g). Similarly, OCP can be used to monitor the real-time charge transfer during PMS activation and organic pollutant degradation on the HDCs electrode surface, without the need for an external potential. As shown in Fig. 4h, the catalyst potential increased rapidly upon the introduction of PMS, then gradually plateaued, indicating the stabilization of the catalyst-PMS complexes. The N–CNT catalyst outperformed the CNT, indicating that PMS could be activated through the SETP mechanism [15]. A two-compartment galvanic oxidation setup (GOP) has recently been introduced, in which PMS and the target pollutant are placed in separate chambers, while the real-time open-circuit potential and current responses are continuously recorded (Fig. 5a) [82]. A large increase in OCP value was conducted upon PMS addition and reached maximum quickly, indicating the efficient electron transfer from PMS to catalysts. Subsequently, a sharp decrease when pollutants (SMX) was added simultaneously. Similarly, enhancement of OCP value in single-chamber system indicated the similar SETP (Fig. 5b). Moreover, the contribution of SETP on SMX degradation could be confirmed as showed inset of Fig. 5b [82].

3.3. Theoretical calculations

DFT calculations offer an efficient way to study PMS activation at the molecular level, focusing on PMS active sites and activation pathways. Generally, PMS adsorption energy (E_{ads}), O–O bond length (I_{O-O}) of activated PMS (PMS*), Gibbs free energy (reaction barrier, $\triangle G$), electron transfer tendency (Q), and charge density difference (CDD) between PMS and HDCs [83]. Dung *et al.* carried out DFT calculations to provide further insights into the PMS adsorption on HDCs, demonstrating the S-doping is more favorable for PMS adsorption than N-doping, with N,S-co-doping exhibits stronger adsorption (Fig. 6a) [84].

However, the lower E_{ads} does not necessarily correlate with higher catalytic performance. And thus, the formation of more ROS confirmed by the enlarger O–O length could be the main reason for PMS activation. Gibbs free energy consists two main stages: (1) dissociation process (E_{dis}); (2) desorption process (E_{des}). The dissociation process could evaluate the generation of $SO_4^{\bullet-*}$, with the more negative E_{dis} value, the more spontaneously the dissociation process occurs. Additionally, the desorption process of $SO_4^{\bullet-}$ to generate free $SO_4^{\bullet-}$, is another important step for PMS activation [85]. For example, in a study by Li *et al.* [23], nitrogen-doped carbon materials were investigated for their role in PMS activation. DFT calculations showed that nitrogen doping lowers the Gibbs free energy of the PMS activation step by stabilizing the transition state and facilitating electron transfer between the PMS molecule and the carbon surface. Specifically, nitrogen atoms, with their

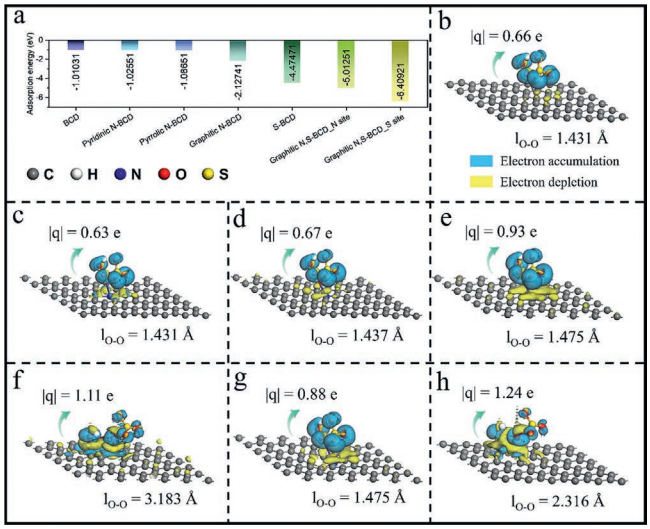


Fig. 6. (a) Adsorption energies of PMS on various biochar derived from durian peel (BCD) models. Charge density difference for (b) pristine BCD, (c) pyrrolic N-doped BCD, (d) pyridinic N-doped BCD, (e) graphitic N-doped BCD, (f) S-doped BCD, (g) N site of graphitic N,S-doped BCD, and (h) S site of graphitic N,S-doped BCD. Reprinted with permission [84]. Copyright 2024, Elsevier.

electron-donating properties, modify the electronic structure of the carbon surface, making it more reactive towards PMS. The presence of nitrogen not only lowers the activation energy for sulfate radical ($SO_4^{\bullet-}$) generation but also shifts the reaction pathway to favor radical generation, as compared to undoped carbon materials. Electron transfer charge (*Q*) and charge density difference (CDD) could visually and directly illustrate the distribution and pathway of charge transfer, further unveiling the interfacial interactions between PMS and HDCs. As shown in Figs. 6b–h, more electrons are transferred from N site of graphitic N,S-BCD or S site of graphitic N,S-BCD to PMS (0.88 or 1.24 e) than pristine BCD (0.66 e), which are consistent with the more electron depletion (yellow region in the CDD image) on the surface of N site of graphitic N,S-BCD or S site of graphitic N,S-BCD [84,86]

4. Environmental applications of HDCs/PMS systems

Natural wastewater contains various types of detergents, surfactants, inorganic salts, dyes, and other substances with complex organic structures, all of which can be harmful to the ecological environment. Inorganic ions could exert an impact on pollutants degradation *via* buffering solution pH, capturing reactive oxygen species and neutralizing electrostatic bonds between reactants. Each kind of anion has its own unique physical and chemical properties, so inorganic anions exhibit obvious influence on the removal of pollutants. In addition, natural organic matter and humic acids also have adverse effects on AOPs.

4.1. Influence of inorganic ions

Coexisting anions in natural waters and wastewaters, even at trace levels, can markedly influence PMS activation—particularly for radical-mediated routes. Common inorganic species (*e.g.*, Cl^-, NO_3^-, SO_4^{2-}, CO_3^{2-}/HCO_3^-, $H_xPO_4^{(x-3)}$ ($x=0$, 1, 2)) differentially impact the Fenton-like performance in the HDCs-catalyzed systems (Text S4 in Supporting information).

Cl^- is the main anion in natural water, and the impact of Cl^- on contaminant degradation depends on the ROS types, their reaction rates with Cl^-, and the specific activation pathways in the system. At low levels, Cl^- can intercept $SO_4^{\bullet-}$ to form $Cl^\bullet$ and $HOCl^{\bullet-}$ [87] with the consumption of $SO_4^{\bullet-}$ and decreasing the oxidation capacity of the PMS-based reaction system [88]. However, HSO_5^- has the ability to oxidize high-level Cl^-, and the hypochlorous acid (HOC) produced during the reaction possesses strong oxidative properties, which aids in the pollutant's removal. When PMS activation is dominated by non-radical pathways, the overall impact of Cl^- is often much less pronounced and can become negligible [89]. NO_3^- showed an inhibitory effect on ECs removal. Low concentration of NO_3^- could slightly inhibited the degradation of organic pollutants due to the consumption of $SO_4^{\bullet-}$ and $^\bullet OH$ by NO_3^-, while excess NO_3^- could adversely enhance the degradation performance of organic pollutants, attributing to the generation of $NO_3^{\bullet-}$. On the other hand, the sulfate anion (SO_4^{2-}) showed improved organic degradation performance, attributed to the efficient generation of $SO_4^{\bullet-}$ due to the increased decomposition rate of PMS. Additionally, the presence of a high dosage of SO_4^{2-} inhibited the transfer of $SO_4^{\bullet-}$ to ·OH, further enhancing the degradation process [90].

More strikingly, CO_3^{2-}, HCO_3^-, and $H_xPO_4^{(x-3)}$ typically have double-effects on the degradation of organic contaminants. Specifically, at the low concentration level, dominated $SO_4^{\bullet-}$ and $^\bullet OH$ could be quenched and generated $CO_3^{\bullet-}$, $HCO_3^{\bullet-}$, and $H_{x-1}PO_4^{\bullet(x-3)}$, which inhibited the oxidation process of organic pollutants [91]. However, a significant amount of alkaline anions can alter the pH of the system to an alkaline condition, promoting the conversion of HSO_5^- to SO_5^{2-} and increasing the production of $^1O_2$ [92].

4.2. Influence of natural organic matter (NOM)

In addition to inorganic anions, natural organic matter is pervasive across diverse water matrices, including municipal wastewater, groundwater, and surface waters [93]. The composition of organic compounds in real water matrices is complex, which makes the impact of organic matter on the PMS-AOP system uncertain. To date, studies have explored the dual effects of organic components on the degradation of emerging contaminants. NOM could compete with target organic pollutants for active species. Additionally, free quinone radicals derived from organic phenols, quinones, and hydroquinone can further activate PMS to generate $SO_4^{\bullet-}$. As is known to all, humic acid (HA), a dominant fraction of natural organic matter, has been reported to inhibit HDC/PMS processes, which is commonly attributed to its abundant carboxyl and phenolic hydroxyl functionalities. Degle *et al.* has proved that the co-existence of HA could suppress sulfacetamide degradation in the $SO_4^{\bullet-}$-dominated nitrogen-doped graphene/PMS system [94]. In systems governed by non-radical pathways (*i.e.*, with minimal involvement of ROS), this inhibitory effect is substantially attenuated [95].

5. Conclusions and perspectives

This article provides an overview of the development of HDCs-based catalysts for PMS activation in pollutant removal. HDCs-based catalysts are considered a new generation of environmentally friendly catalysts, owing to their excellent adsorption capacity, tunable coordination environment, metal-free nature, and their ability to prevent secondary pollution caused by metal leaching during the PMS activation process. However, several key issues still need to be addressed:

(1) Research on specific HDC-based catalysts with uniform active sites, defects, porosity, and other characteristics related to PMS activation mechanisms is ongoing. The design and synthesis of HDC-based catalysts often rely on trial and error, a process that is time-consuming and costly. To address this, automated machine learning (ML) techniques have been

employed to develop catalyst models and better understand the PMS activation process. However, the application of ML for modeling HDC-based catalyst structures in PMS activation for organic pollutant removal remains limited. Future research is needed to provide alternative approaches for modeling the reactivity of HDC-based catalysts, focusing on the relationship between structural descriptors and reactivity properties.

(2) Deep investigation of surface activation mechanisms should be conducted. At present, the recognized reaction mechanisms encompass radical pathways driven by $SO_4^{\bullet-}$, which leads to the generation of $^{\bullet}OH$, non-radical pathways triggered by $^1O_2$, and direct degradation through the surface electron transfer process (SETP). However, the activation mechanism that includes surface-bound complexes of PMS and catalysts has not been investigated yet. The generation of $^1O_2$ during PMS activation remains uncertain, and further research is necessary to pinpoint reliable active sites. Although both radical and non-radical pathways may be present in various systems, usually one pathway dominates. Understanding the reasons for this dominance and its dynamic interaction with HDCs-based catalysts or specific contaminants warrants further study.

(3) Greater emphasis should be placed on feasibility analysis of practical applications. The long-term durability and reusability of HDC-based catalysts are essential for their practical application. Over time, several factors contribute to the decline in catalytic performance. A key issue is the gradual loss of catalytic activity, primarily due to the depletion of surface-active sites. Additionally, intermediate degradation products can accumulate on the catalyst surface, obstructing active sites and clogging the porous structure, which in turn diminishes the catalyst's effectiveness. Furthermore, the adsorption of PMS or organic pollutants onto the catalyst surface can trigger surface oxidation reactions, reduce the availability of active sites and decrease the specific surface area of the catalyst. While heat treatment and other regeneration techniques can remove some of these blocking products and partially restore active sites, these methods may not fully address the long-term demands for stable catalytic performance. To improve the durability and reusability of HDC-based catalysts, further research is needed to develop more effective strategies.

(4) Assessing the environmental impacts of deploying HDC-based catalysts for PMS activation. At present, the environmental impact of using HDCs-based catalysts in full-scale systems is not well understood. To address this, comprehensive life-cycle assessment (LCA) is needed to quantify the overall footprint of these catalysts and to systematically appraise their potential environmental impacts, including their behavior during use, disposal, and possible degradation. Long-term ecological effects should be evaluated *via* a comprehensive analysis. And thus, more researches should be focused to fill this knowledge gap by assessing the environmental risks associated with HDCs-based catalysts/PMS systems, ultimately helping to minimize their environmental impact and ensuring their safe and sustainable application in large-scale systems

CRediT authorship contribution statement

Sai Bai: Writing – review & editing, Writing – original draft, Formal analysis, Conceptualization. **Qianyu Pan:** Formal analysis. **Xiangning Xu:** Resources. **Minxian Cheng:** Software, Formal analysis. **Xiaoming Peng:** Supervision. **Jin Qian:** Visualization, Supervision, Project administration.

Declaration of competing interest

The authors declare that they have no known competing financial interests or personal relationships that could have appeared to influence the work reported in this paper.

Acknowledgments

This work was financially supported by the National Natural Science Foundation of China (No. 52470088), Natural Science Foundation of Sichuan Province (No. 25NSFSC0854), Guangdong Basic and Applied Basic Research Foundation (No. 2024A1515030032), and Natural Science Foundation of Shenzhen (No. JCYJ20220530161806014).

Supplementary materials

Supplementary material associated with this article can be found, in the online version, at doi:10.1016/j.cclet.2026.112502.

References

[1] X. Chen, W.D. Oh, T.T. Lim, Chem. Eng. J. 354 (2018) 941–976.
[2] M. Priyadarshini, I. Das, M.M. Ghangrekar, L. Blaney, J. Environ. Manage. 316 (2022) 115295.
[3] X. Lei, H. Zhao, C. Bai, et al., Chin. Chem. Lett. 36 (2025) 111550.
[4] D. Yu, M. Wu, Q. Hu, et al., J. Hazard. Mater. 367 (2019) 456–464.
[5] L. Qin, Z. Wang, Y. Fu, et al., J. Hazard. Mater. 414 (2021) 125448.
[6] C. Lai, F. Xu, M. Zhang, et al., J.Colloid Interf. Sci. 588 (2021) 283–294.
[7] F. Qin, Y. Peng, G. Song, et al., J. Hazard. Mater. 398 (2020) 122816.
[8] R. Huang, J. Yang, Y. Cao, et al., Sep. Purif. Technol. 291 (2022) 120963.
[9] S. Wacławek, H.V. Lutze, K. Grübel, et al., Chem. Eng. J. 330 (2017) 44–62.
[10] Q. Tian, J. Chang, X. Peng, et al., Angew. Chem. Int. Ed. 64 (2025) e202503995.
[11] X. Zhou, Z. Zeng, G. Zeng, et al., Chem. Eng. J. 383 (2020) 123091.
[12] Y. Zhang, S. Liu, D. Chen, X. Xu, Chin. Chem. Lett. 35 (2024) 108666.
[13] Q. Tian, B. Yu, Z. Li, et al., Chin. Chem. Lett. 36 (2025) 110322.
[14] Y. Wang, X. Duan, Y. Xie, et al., ACS Catal. 10 (2020) 13383–13414.
[15] W. Ren, G. Nie, P. Zhou, et al., Environ. Sci. Technol. 54 (2020) 6438–6447.
[16] G. Wang, S. Chen, X. Quan, et al., Carbon 115 (2017) 730–739.
[17] D. Li, X. Duan, H. Sun, et al., Carbon 115 (2017) 649–658.
[18] I.Y. Jeon, H.J. Noh, J.B. Baek, Chem. Asian J. 15 (2020) 2282–2293.
[19] W.J. Lee, J. Lim, S.O. Kim, Small Methods 1 (2017) 1600014.
[20] D. Guo, R. Shibuya, C. Akiba, et al., Science 351 (2016) 361–365.
[21] J. Kang, X. Duan, L. Zhou, et al., Chem. Eng. J. 288 (2016) 399–405.
[22] X. Huang, F. Li, X. Zhang, et al., Sep. Purif. Technol. 354 (2025) 129003.
[23] W. Li, C. Nie, X. Wang, et al., Sep. Purif. Technol. 323 (2023) 124418.
[24] X. Duan, Z. Ao, H. Sun, et al., ACS Appl. Mater. Interfaces 7 (2015) 4169–4178.
[25] Y. Gao, T. Li, Y. Zhu, et al., J. Hazard. Mater. 393 (2020) 121280.
[26] Z. Sun, L. Zhao, C. Liu, et al., Environ. Sci. Technol. 53 (2019) 10342–10351.
[27] L. Xu, C. Wu, P. Liu, et al., Chem. Eng. J. 387 (2020) 124065.
[28] J. Liu, T. Liang, R. Tu, et al., Appl. Surf. Sci. 481 (2019) 344–352.
[29] K. Fujisawa, T. Hayashi, M. Endo, et al., Nanoscale 10 (2018) 12723–12733.
[30] Y. Wang, M. Liu, X. Zhao, et al., Carbon 135 (2018) 238–247.
[31] S. She, Y. Wang, R. Chen, et al., Chemosphere 266 (2021) 128929.
[32] D. Yang, L. Zhao, X. Feng, et al., Funct. Mater. Lett. 14 (2021) 2151019.
[33] Z. Yang, Z. Yao, G. Li, et al., ACS Nano 6 (2012) 205–211.
[34] M. Huang, X. Wang, C. Liu, et al., J. Environ. Chem. Eng. 9 (2021) 106536.
[35] Y. Guo, Z. Zeng, Y. Zhu, et al., Appl. Catal. B: Environ. 220 (2018) 635–644.
[36] Y. Guo, Z. Zeng, Y. Li, et al., Catal. Today 307 (2018) 12–19.
[37] X. Mo, D.E. López, K. Suwannakarn, et al., J. Catal. 254 (2008) 332–338.
[38] S. Liu, C. Lai, B. Li, et al., Chem. Eng. J. 384 (2020) 123304.
[39] E. Cruz-Silva, D.A. Cullen, L. Gu, et al., ACS Nano 2 (2008) 441–448.
[40] I.O. Maciel, J. Campos-Delgado, E. Cruz-Silva, et al., Nano Lett. 9 (2009) 2267–2272.
[41] K. Zhang, X. Min, T. Zhang, et al., J. Hazard. Mater. 413 (2021) 125294.
[42] X. Liang, Y. Zhao, B. Liu, et al., Sep. Purif. Technol. 340 (2024) 126739.
[43] T. Wang, L. Xue, L. Zheng, et al., J. Hazard. Mater. 416 (2021) 126126.
[44] X. Duan, K. O'Donnell, H. Sun, et al., Small 11 (2015) 3036–3044.
[45] X. Li, J. Wang, X. Duan, et al., ACS Catal. 11 (2021) 4848–4861.
[46] X. Chen, X. Duan, W.D. Oh, et al., Appl. Catal. B: Environ. 253 (2019) 419–432.
[47] P. Sun, H. Liu, M. Feng, et al., Appl. Catal. B: Environ. 251 (2019) 335–345.
[48] H.R. Ghenaatian, M. Shakourian-Fard, G. Kamath, J. Mater. Sci. 54 (2019) 13175–13189.
[49] X. Duan, K. O'Donnell, H. Sun, et al., Small 11 (2015) 3036–3044.
[50] J. Shi, N. Yan, H. Cui, et al., ACS Sustainable Chem. Eng. 7 (2019) 19513–19521.
[51] O.V. Sedelnikova, Y.V. Fedoseeva, A.I. Romanenko, et al., Carbon 143 (2019) 660–668.
[52] Y. Zhao, L. Yang, S. Chen, et al., J. Am. Chem. Soc. 135 (2013) 1201–1204.
[53] T. Schiros, D. Nordlund, L. Palova, et al., ACS Nano 10 (2016) 6574–6584.
[54] M. Rafique, Y. Shuai, I. Ahmed, et al., Appl. Surf. Sci. 480 (2019) 463–471.

[55] S. Some, J. Kim, K. Lee, et al., Adv. Mater. 24 (2012) 5481–5486.
[56] Y. Zhang, K. Cui, X. Liu, et al., Sep. Purif. Technol. 359 (2025) 130545.
[57] X. Xin, H. Kang, J. Feng, et al., Chem. Eng. J. 393 (2020) 124710.
[58] X. Qiao, S. Liao, C. You, R. Chen, Catalysts 5 (2015) 981–991.
[59] S. Chen, T. Liu, S.O. Olanrele, et al., J. Energy Chem. 54 (2021) 143–150.
[60] C. Fu, G. Sun, G. Yin, et al., Sep. Purif. Technol. 292 (2022) 120922.
[61] J. Yang, D. Zeng, Q. Zhang, et al., Appl. Catal. B: Environ. 279 (2020) 119363.
[62] E.T. Yun, J.H. Lee, J. Kim, et al., Environ. Sci. Technol. 52 (2018) 7032–7042.
[63] Y. Lei, Y. Yu, X. Lei, et al., Environ. Sci. Technol. 57 (2023) 5433–5444.
[64] W. Ren, C. Cheng, P. Shao, et al., Environ. Sci. Technol. 56 (2022) 78–97.
[65] J. Wu, J. Wang, C. Liu, et al., Environ. Sci. Technol. 56 (2022) 13996–14007.
[66] Z.H. Xie, C.S. He, H.Y. Zhou, et al., Environ. Sci. Technol. 56 (2022) 8784–8795.
[67] Y. Gao, T. Wu, C. Yang, et al., Angew. Chem. Int. Ed. 60 (2021) 22513–22521.
[68] Y.J. Zhang, J.J. Chen, H.Q. Yu, Chem. Eng. J. 446 (2022) 137237.
[69] P. Shao, Y. Jing, X. Duan, et al., Environ. Sci. Technol. 55 (2021) 16078–16087.
[70] R. Yin, W. Guo, H. Wang, et al., Chem. Eng. J. 334 (2018) 2539–2546.
[71] Y. Yang, G. Banerjee, G.W. Brudvig, et al., Environ. Sci. Technol. 52 (2018) 5911–5919.
[72] D. Yu, J. He, T. Xie, et al., J. Hazard. Mater. 442 (2023) 130085.
[73] P. Yang, Y. Long, W. Huang, D. Liu, Appl. Catal. B: Environ. 324 (2023) 122245.
[74] B. Li, H.Y. Xu, G.H.N. Chi, et al., Chem. Eng. J. 483 (2024) 149403.
[75] Y.J. Zhang, G.X. Huang, L.R. Winter, et al., Nat. Commun. 13 (2022) 3005.
[76] M. Kohantorabi, G. Moussavi, S. Giannakis, Chem. Eng. J. 411 (2021) 127957.
[77] S. Tian, Y. Xu, Y. Ma, et al., Chem. Eng. J. 485 (2024) 150016.
[78] P. Duan, M. Li, X. Xu, et al., Appl. Catal. B: Environ. 344 (2024) 123619.
[79] T. Zhang, Y. Chen, Y. Wang, et al., Environ. Sci. Technol. 48 (2014) 5868–5875.
[80] Y. Chen, H. Kang, M. Cheng, et al., Adv. Funct. Mater. 34 (2024) 2309223.
[81] F. Qi, Z. Zeng, Q. Wen, Z. Huang, J. Hazard. Mater. 416 (2021) 125810.
[82] J. Miao, Y. Zhu, Y. Wei, et al., J. Hazard. Mater. 465 (2024) 133344.
[83] C. Chu, J. Yang, X. Zhou, et al., Environ. Sci. Technol. 55 (2021) 1242–1250.
[84] N.T. Dung, V.D. Thao, N.P. Thao, et al., Chem. Eng. J. 483 (2024) 149099.
[85] J. Qi, X. Yang, P.Y. Pan, et al., Environ. Sci. Technol. 56 (2022) 5200–5212.
[86] N.T. Dung, T.C. Khiem, N.P. Thao, et al., Chemosphere 361 (2024) 142452.
[87] H. Xue, S. Gao, M. Li, et al., Environ. Res. 188 (2020) 109804.
[88] W. Peng, Y. Fu, L. Wang, et al., Chin. Chem. Lett. 32 (2021) 2544–2550.
[89] C. Zhao, B. Shao, M. Yan, et al., Chem. Eng. J. 416 (2021) 128829.
[90] Y. Yang, G. Banerjee, G.W. Brudvig, et al., Environ. Sci. Technol. 52 (2018) 5911–5919.
[91] S. Xiao, M. Cheng, H. Zhong, et al., Chem. Eng. J. 384 (2020) 123265.
[92] Y.H. Guan, J. Ma, Y.M. Ren, et al., Water Res. 47 (2013) 5431–5438.
[93] Y. Wang, Y. Deng, L. Yao, X. Yang, Water Res. 248 (2024) 120880.
[94] V.L. Dagle, G. Collinge, M. Rahman, et al., Appl. Catal. B: Environ. 331 (2023) 122707.
[95] J. Lee, U. von Gunten, J.-H. Kim, Environ. Sci. Technol. 54 (2020) 3064–3081.